J Adv Ceram

Research Article

Multi-anion sublattice engineering enables exceptional ablation-resistant performance in $Hf_{0.8}Zr_{0.2}B_{0.1}C_{0.5}N_{0.4}$–SiC ultra-high temperature ceramics

Xiaoyu Wang[1,2,3], Dewei Ni[1,2,4,✉], Bowen Chen[1,2], Feiyan Cai[1,2], Yang Hu[1,2,3], Yanmei Kan[1,2], Yusheng Ding[1,2], Shaoming Dong[1,2]

Cite this article: Wang X, Ni D, Chen B, et al. *J Adv Ceram* 2026, **15**(8): 9221347. https://doi.org/10.26599/JAC.2026.9221347

ABSTRACT: High-entropy ultrahigh temperature ceramics (UHTCs) have garnered significant attention for their outstanding designability and performance, yet existing strategies remain largely confined to cationic sublattice engineering, leaving the potential of anionic site manipulation unexplored. Herein, we extend the entropy-stabilization paradigm to the anion sublattice by designing a multianion $Hf_{0.8}Zr_{0.2}B_{0.1}C_{0.5}N_{0.4}$ solid solution. The resulting $Hf_{0.8}Zr_{0.2}B_{0.1}C_{0.5}N_{0.4}$–SiC ceramic achieves negative ablation rates (–0.049 and –0.287 μm·s^{-1}) under 2600 °C plasma flame exposure, markedly outperforming $Hf_{0.8}Zr_{0.2}C$–SiC. This exceptional ablation-resistant performance originates from the synergistic effects enabled by multianion sublattice engineering. The incorporation of B–C–N intrinsically enhances fracture toughness, while *in situ* precipitation of hexagonal graphite during ablation extrinsically arrests cracks through interfacial shear, preventing catastrophic disintegration. Furthermore, the multianion matrix undergoes a sequential oxidation process, forming an HfZrBCNO interlayer that acts as an oxygen scavenger. Concurrently, *h*-BN precipitates at grain boundaries, serving as compliant diffusion barriers that impede oxygen ingress into SiC. This dual-layer protection mechanism suppresses the active oxidation of SiC (SiC + O_2 → SiO + CO) and promotes the formation of a dense, scouring-resistant $HfZrO_2$–SiO_2 composite barrier. By demonstrating simultaneous microstructural toughening and mesoscale oxidation management, this work establishes multianion sublattice engineering as a transformative platform for designing next-generation thermal protection materials beyond the limits of conventional entropy-stabilized ceramics.

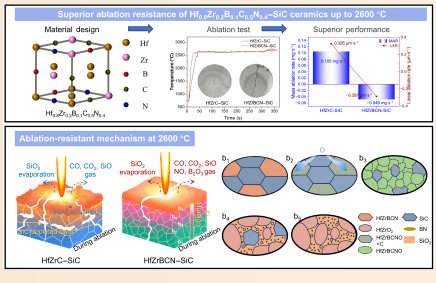

KEYWORDS: multianion engineering; ablation resistance; fracture toughening; active oxidation; ultrahigh temperature ceramics (UHTCs)

1 Introduction

Hypersonic vehicles represent a critical frontier in aerospace development [1,2]. As the flight speed increases, aerodynamic heating becomes more severe, causing surface temperatures to rise dramatically above 2000 °C within a short period [3,4]. Under such harsh conditions, conventional refractory materials undergo catastrophic failure, necessitating the development of ultrahigh temperature ceramics (UHTCs) and composites with exceptional ablation resistance [5,6].

UHTCs—typically comprising carbides, borides, and nitrides of Group IVB and VB transition metals—exhibit melting points exceeding 3000 °C and exceptional chemical stability [7,8]. Among these, Hf/Zr-based UHTCs are particularly promising for leading-edge and nose-cone applications due to the formation of refractory oxidation products (HfO_2: 2900 °C and ZrO_2: 2677 °C) with low vapor pressures [9,10]. However, the oxides formed from UHTCs tend to develop porous layers that provide inadequate protection. The incorporation of SiC particles can inhibit abnormal grain growth of UHTC grains, promote densification, and thereby effectively enhance the flexural strength and fracture toughness of the material. Furthermore, the addition of SiC forms a protective SiO_2 layer through passive oxidation (SiC + $2O_2$ → SiO_2 + CO_2) [11–13]. The low-melting-point silica glass phase binds solid particles and fills pores, with the dense oxide layer reducing further contact between surface oxygen and the substrate, thus significantly decreasing ablation mass loss [14]. Nevertheless, when the SiC content is too low, insufficient high-

[1] State Key Laboratory of High Performance Ceramics, Shanghai Institute of Ceramics, Chinese Academy of Sciences, Shanghai 200050, China. [2] Structural Ceramics and Composites Engineering Research Center, Shanghai Institute of Ceramics, Chinese Academy of Sciences, Shanghai 200050, China. [3] University of Chinese Academy of Sciences, Beijing 100049, China. [4] Hangzhou Institute for Advanced Study, University of Chinese Academy of Sciences, Hangzhou 310024, China.

✉ Corresponding author. E-mail: deweini@mail.sic.ac.cn

Received: April 23, 2026; Revised: July 8, 2026; Accepted: July 9, 2026

viscosity SiO_2 glass phase is generated within the oxide scale, failing to effectively bind refractory oxide particles, fill thermally induced cracks, or resist high-speed gas flow erosion; conversely, excessive SiC content results in an increased liquid phase within the oxide layer that is readily washed away by high-speed plasma gas flow [15]. Moreover, at the interface beneath the oxide scale, the combination of high temperatures and low oxygen partial pressure creates thermodynamic conditions favorable for the active oxidation of SiC ($SiC + O_2\uparrow \rightarrow SiO\uparrow + CO\uparrow$) [16,17]. The resulting gaseous SiO rapidly volatilizes, generating porous SiC-depleted layers that compromise structural integrity and accelerate ablative mass loss [18,19]. A SiC content of 30 vol% ensures sufficient SiO_2 glass to bind refractory oxide particles and fill cracks while avoiding excessive liquid-phase loss under high-velocity plasma flow [20,21].

Recently, some researchers have attempted to introduce multiple elements into the cation sublattice to form high-entropy ceramics (HECs) [22–24]. These materials benefit from the typical characteristics of severe lattice distortion and sluggish diffusion in high-entropy configurations, thereby exhibiting excellent mechanical strength and oxidation resistance [25–27]. Moreover, incorporating certain elements (e.g., Ti and Nb) may introduce volatile, low-melting-point oxides (TiO_2: 1843 °C and Nb_2O_5: 1512 °C) during ablation [28,29]. Under extreme heat flux, these oxides rapidly volatilize, compromising the integrity of the protective scale and potentially leading to catastrophic failure [30,31]. As research on the principal cation elements of ultrahigh temperature ceramics approaches its limitations, some researchers have turned to anion doping. Zeng *et al.* [32] developed C/C–$(Zr_{0.8}Ti_{0.2})(C_{0.74}B_{0.26})$ composites with superior ablation resistance, whose performance is several times better than that of ZrC, ZrB_2, and their composites. Additionally, the incorporation of boron results in a more negative binding energy for (Zr,Ti)C, reducing its oxidation rate by 30% at 1600 °C in air [33]. Furthermore, the introduction of nitrogen also demonstrates significant advantages. Recent calculations identify $HfC_{0.75}N_{0.22}$ as the highest-melting compound (~4400 K), owing to nitrogen-induced stabilization of the solid phase relative to the liquid [34–36]. Moreover, the presence of nitrogen atoms in hafnium carbonitride elevates the oxygen adsorption energy barrier of metal atoms, resulting in mass/linear ablation losses for $Hf(C_{0.76}N_{0.24})$ being reduced by 89.1%/90.9% compared with HfC [37].

Therefore, the simultaneous incorporation of B and N anions into carbides may effectively enhance their performance [38]. Guan *et al.* [39] first synthesized BCN multianion UHTC powders via mechanical alloying using metals, hexagonal boron nitride (h-BN), and graphite. However, this method suffers from two drawbacks: (i) The high energy input generates numerous fresh metal surfaces that readily react with residual oxygen during ball milling, producing oxide impurities [40]; and (ii) excessive boron content exceeds the structural tolerance of the rock-salt solid solution, leading to precipitation of hexagonal transition metal diborides, as transition metal diborides adopt a hexagonal structure markedly distinct from cubic carbides/nitrides [41]. Recently, Lun *et al.* [42] utilized carbon vacancies in nonstoichiometric $(Zr,Hf,Ti)C_x$ as diffusion channels to fabricate single-phase face-centered cubic (FCC) $(Zr_{0.3}Hf_{0.5}Ti_{0.2})(C_{0.87}B_{0.03}N_{0.07})$ with B_2O_3 and g-C_3N_4 as boron and nitrogen sources. Trace B and N incorporation enhanced the binding energy and elevated the oxidation onset temperature from 475 to 520 °C, demonstrating that the B–C–N design confers significantly enhanced structural stability and oxidation resistance.

In our previous work, $Hf_{0.8}Zr_{0.2}B_{0.1}C_{0.5}N_{0.4}$ powder was synthesized at 1400 °C via carbothermal-borothermal reduction ($0.8HfO_2 + 0.2ZrO_2 + 0.05B_4C + 2.45C + 0.2N_2\uparrow \rightarrow Hf_{0.8}Zr_{0.2}B_{0.1}C_{0.5}N_{0.4} + 2CO\uparrow$), using HfO_2 and ZrO_2 as cation sources and B_4C, carbon black, and N_2 as boron, carbon, and nitrogen sources, respectively. The product exhibited a composition consistent with the nominal design and homogeneous elemental distribution [43]. Building upon this, we herein fabricate dense $Hf_{0.8}Zr_{0.2}B_{0.1}C_{0.5}N_{0.4}$–SiC ceramics (denoted HfZrBCN–SiC) via hot pressing to elucidate the protective efficacy of the B–C–N solid solution in bulk systems, employing $Hf_{0.8}Zr_{0.2}C$–SiC ceramics (denoted as HfZrC–SiC) as a reference. Systematic ablation testing at 2600 °C reveals that the multianion entropy engineering strategy achieves exceptional ablation resistance through hierarchical protection: (i) Microscale toughening, wherein B–C–N incorporation intrinsically enhances fracture toughness synergizing with graphite precipitation that deflects cracks and dissipates energy through interfacial shear, and (ii) mesoscale oxidation management via sequential formation of HfZrBCNO (oxygen scavenging) and *h*-BN (diffusion blocking), which collectively suppress SiC active oxidation and facilitate the formation of a dense composite oxide layer. This work establishes anion entropy engineering as a paradigm for designing next-generation UHTCs with enhanced ablation resistance and suppressed active oxidation.

2 Experimental

2.1 Materials synthesis and processing

ZrO_2 (1–3 μm, 99.9%), HfO_2 (1–3 μm, 99.9%), B_4C (2–4 μm, 99.9%) (Shanghai Aladdin Biochemical Technology Co., Ltd.), and carbon black (50 nm, 99.9%, Shanghai St-nano Science & Technology Co., Ltd.) were used as raw materials. The starting materials were weighed according to target stoichiometries and ball-milled with ZrO_2 media in ethanol for 8 h. The resulting slurries were dried, sieved, and transferred into graphite crucibles. $Hf_{0.8}Zr_{0.2}B_{0.1}C_{0.5}N_{0.4}$ was synthesized at 1600 °C in flowing N_2 for 2 h, whereas $Hf_{0.8}Zr_{0.2}C$ was prepared under an Ar atmosphere. Detailed synthesis and fabrication procedures have been reported in our previous work [43].

Subsequently, 30 vol% SiC (100–150 nm, 99.9%) was incorporated into the synthesized powders. The mixtures were subsequently ball-milled using SiC media in ethanol for 12 h. After drying, the composite powders were loaded into graphite dies and densified via hot pressing at 2100 °C under 30 MPa for 60 min in vacuum (heating rate: 10 °C·min^{-1}). The resulting ceramics were labeled HfZrBCN–SiC and HfZrC–SiC, respectively.

2.2 Mechanical characterization

The Vickers microhardness (HV_{30}) of the sintered bulk was measured using a hardness tester (Tukon-2100B, Instron, USA) under an applied load of 294.3 N (30 kgf) with dwell time of 15 s. The indentation length was measured by optical microscopy, and the fracture toughness was determined by the indentation method: $K_{IC} = 0.15(HV_{30}/\sum_{i=1}^{4} l_i)^{1/2}$, where K_{IC} is the fracture toughness (MPa·m$^{1/2}$) and l_i is the Vickers indentation crack length (mm).

2.3 Ablation resistance evaluation

Ablation resistance was evaluated using an air plasma system (QHKJ-DLZ50, Beijing Qinhe Technology Co., Ltd., China). A plasma flame was generated using a gas mixture of air

(~0.5 $m^3 \cdot h^{-1}$) and nitrogen (~2.7 $m^3 \cdot h^{-1}$). Tests were conducted at a surface temperature of 2600 °C for 300 s. The surface temperature was monitored using a bichromatic (two-color) infrared pyrometer (RATMAR1SCSF, Raytek, USA). Changes in mass and thickness at the ablation center were measured using an electronic balance (precision: ±0.0001 g) and a micrometer (precision: ±0.01 mm), respectively. The linear ablation rate (LAR) and mass ablation rate (MAR) were calculated based on $LAR = (l_0 - l_t)/\Delta t$ and $MAR = (m_0 - m_t)/\Delta t$, respectively, where l_0 and l_t are the thicknesses of the ablation center before and after ablation (μm), respectively; m_0 and m_t are the masses of the sample before and after ablation (mg), respectively; Δt is the ablation time (s).

2.4 Microstructural analysis

The bulk density and open porosity of the samples were determined by the Archimedes method. Phase composition was analyzed by an X-ray diffractometer (XRD; Ultima IV, Rigaku Corporation, Japan). For ablated surfaces, localized phase distributions were characterized using a microfocus two-dimensional X-ray diffractometer (D8 DISCOVER, Bruker, Germany). Surface roughness was quantified using an optical profilometer (MarSurf LD130, Mahr, Germany). The microstructure was examined using a field-emission scanning electron microscope (FESEM; Merlin Compact, Zeiss, Germany) equipped with an energy-dispersive spectrometer (EDS; Xplore 30, Oxford Instruments, UK) and an electron backscatter diffractometer (EBSD; INCA Series, Oxford Instruments, UK). Elemental distribution was determined by an electron probe microanalyzer (EPMA; JEOL-JXA-8530F, Japan). High-resolution transmission electron microscopy (HRTEM), selected area electron diffraction (SAED), and EDS were performed using a spherical aberration-corrected transmission electron microscope (TEM; HF5000, Hitachi, Japan). TEM samples of the ablated composite were prepared by focused ion beam (FIB; Versa 3D, FEI, USA) using the *in situ* lift-out technique.

3 Results and discussion

3.1 Fabrication and microstructure of HfZrBCN–SiC ceramics

Figure 1 presents the physical properties, phase composition, and microstructural characteristics of hot-pressed HfZrBCN–SiC and HfZrC–SiC ceramics. As shown in Fig. 1(a), both composites exhibit low apparent porosity, indicating successful densification at 2100 °C. Notably, HfZrBCN–SiC achieves higher densification (8.68 $g \cdot cm^{-3}$) with lower porosity (4.10%) than HfZrC–SiC (8.13 $g \cdot cm^{-3}$ and 6.53% porosity). This enhanced sinterability is primarily attributed to the increased configurational entropy of the B–C–N anionic solid solution. According to the configurational entropy equation $S_{SL}^{config} = -R\sum_s \sum_i a^s X_i^s \ln(X_i^s) / \sum_s a^s$, where a^s is the number of sites on the s sublattice; X_i^s is the fraction of element species i randomly distributed on the s sublattice; R is the gas constant [44,45], the S_{SL}^{config} of $Hf_{0.8}Zr_{0.2}B_{0.1}C_{0.5}N_{0.4}$ is 1.45R, significantly exceeding that of $Hf_{0.8}Zr_{0.2}C$ (0.5R). This higher configurational entropy effectively lowers the critical sintering temperature according to the relationship $(T_S = (\Delta H_{mix} - \Delta G_{mix})/\Delta S_{config}$, where T_S is the critical sintering temperature; ΔH_{mix} is the difference in mixing enthalpy; ΔG_{mix} is the change in Gibbs free energy; ΔS_{config} is the configurational entropy) [46,47]. The metallic luster observed in the polished samples (insets of Fig. 1(a)) further confirms the achievement of full densification. Interestingly, HfZrC–SiC exhibits a silvery-white appearance, whereas HfZrBCN–SiC displays a characteristic dark purple color, similar to that of Ta_4HfC_5, a compound historically known for its high melting

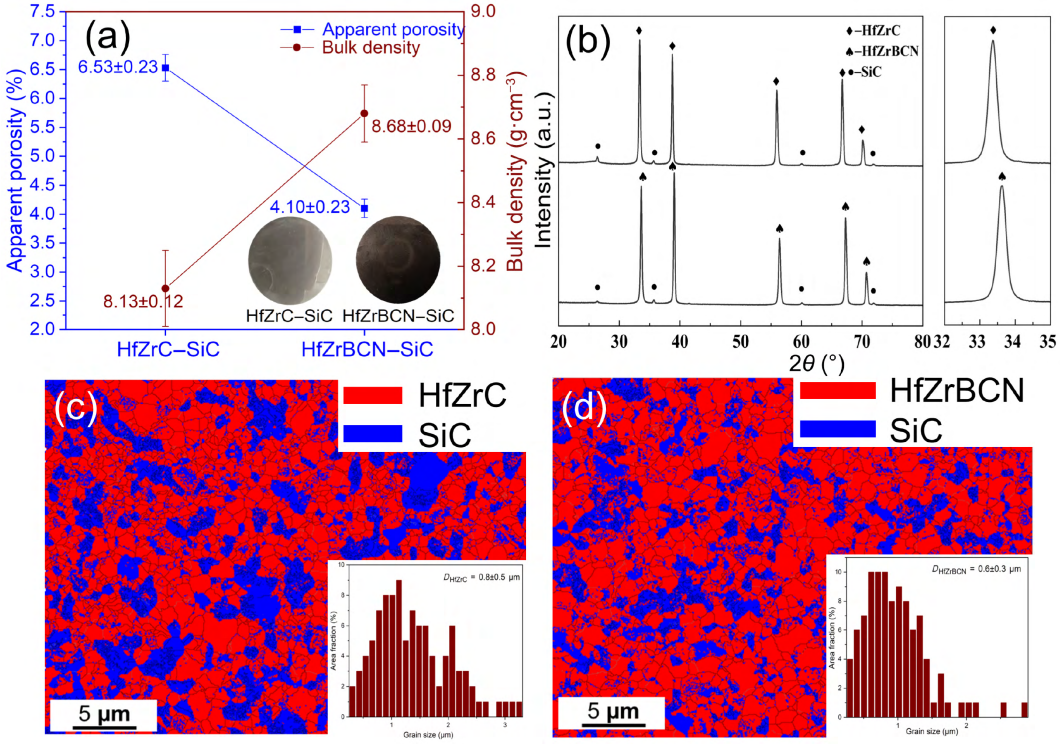

Fig. 1 (a) Bulk density and apparent porosity of HfZrC–SiC and HfZrBCN–SiC ceramics; (b) XRD patterns of HfZrC–SiC and HfZrBCN–SiC ceramics; phase distribution maps of as-sintered (c) HfZrC–SiC and (d) HfZrBCN–SiC ceramics. Insets in (a) show digital photographs of samples, while insets in (c, d) display grain size distributions of HfZrC and HfZrBCN matrices, respectively.

point [48]. This color difference arises from visible light reflection governed by electronic transitions between ground and excited states, which are modified by B and N doping [49].

XRD analysis (Fig. 1(b)) confirms that no reactions occurred between SiC and UHTC phases. The HfZrBCN–SiC composite primarily consists of the HfZrBCN solid solution and SiC, while HfZrC–SiC comprises HfZrC and SiC. Compared with those of HfZrC, the diffraction peaks of HfZrBCN shift to higher angles. This shift is attributed to the smaller ionic radius of nitrogen, which, together with the higher nitrogen doping level relative to boron, results in a smaller lattice constant of HfZrBCN.

Phase distribution maps (Figs. 1(c) and 1(d)) reveal uniform SiC dispersion (blue regions) within both matrices. HfZrBCN–SiC exhibits a marginally refined grain structure (HfZrBCN matrix ~0.6 μm versus HfZrC matrix ~0.8 μm) with enhanced microstructural homogeneity. This modest grain retention combined with improved densification arises from the sluggish diffusion effect: The incorporation of B and N raises the activation energy for atomic diffusion, effectively decoupling pore elimination from grain-boundary migration [50]. While sufficient atomic mobility under hot-pressing conditions facilitates higher density, the sluggish grain-boundary motion suppresses coarsening during the final sintering stage, yielding a dense yet fine-grained architecture [51].

Figure 2 presents the mechanical properties and fracture characteristics of the as-sintered ceramics. Benefiting from enhanced densification and lattice-distortion hardening from B and N incorporation [52–54], HfZrBCN–SiC achieves a Vickers hardness of 17.44±0.17 GPa, a 9.20% increase over HfZrC–SiC (15.97±0.17 GPa). Concurrently, the fracture toughness improves from 3.08±0.14 to 5.02±0.21 MPa·m$^{1/2}$ (a 62.99% enhancement). This substantial toughening arises from the synergistic interplay of anion sublattice engineering and microstructural refinement. The incorporation of N introduces lower bond energy M–N bonds that partially replace rigid M–C bonds, disrupting the highly rigid covalent network and conferring local deformability that allows crack-tip energy dissipation via bond reorganization and blunting [47,55,56]. Concurrently, the sluggish diffusion refines the grain structure, promoting intergranular fracture and activating extrinsic toughening mechanisms such as crack deflection and grain bridging (Fig. 2(b)) [46,57].

3.2 Ablation-resistant performance of HfZrBCN–SiC ceramics up to 2600 °C

The ablation resistance of HfZrC–SiC and HfZrBCN–SiC ceramics was evaluated under a plasma flame at 2600 °C for 300 s. Post-ablation macromorphologies are presented in Fig. 3(a). Both HfZrC–SiC and HfZrBCN–SiC surfaces exhibit white oxide layers, which serve as the first line of defense against thermal shock. However, without effective energy dissipation, phase transformations and thermal stresses accumulate within these layers, leading to crack initiation. The underlying HfZrC–SiC is inherently brittle and lacks mechanisms to resist crack propagation. In contrast, HfZrBCN–SiC fractures into only two halves owing to the toughening effect, which will be discussed in Section 3.3.

Figure 3(b) quantifies the ablation-resistant performance. Strikingly, HfZrBCN–SiC exhibits negative ablation rates (MAR: −0.049 mg·s^{-1} and LAR: −0.287 μm·s^{-1}), indicating net material gain. This occurs because oxide formation outpaces volatilization losses (CO, CO_2, and SiO). Consequently, the dense oxide layer grows outward faster than surface recession, resulting in a negative linear ablation rate. This demonstrates the superior ablation-resistant performance of HfZrBCN–SiC. Furthermore, three-dimensional (3D) surface profilometry (Figs. 3(c) and 3(d)) corroborates this result. HfZrBCN–SiC exhibits a significantly flatter surface, indicating effective resistance to plasma erosion, while HfZrC–SiC displays a rougher surface corresponding to deeper ablation and more severe material removal.

Figure 4 presents the phase composition and surface morphologies of the ablated ceramics at different regions (ablation center, transition area, and ablation edge). Combined XRD analysis (Figs. 4(a) and 4(e)) reveals that both HfZrC–SiC and HfZrBCN–SiC form oxide layers composed of solid-phase $HfZrO_2$ and glassy SiO_2. EPMA mapping (Fig. 4(i)) further demonstrates that large $HfZrO_2$ particles serve as the oxide skeleton, providing structural support. The SiO_2 glass phase acts as

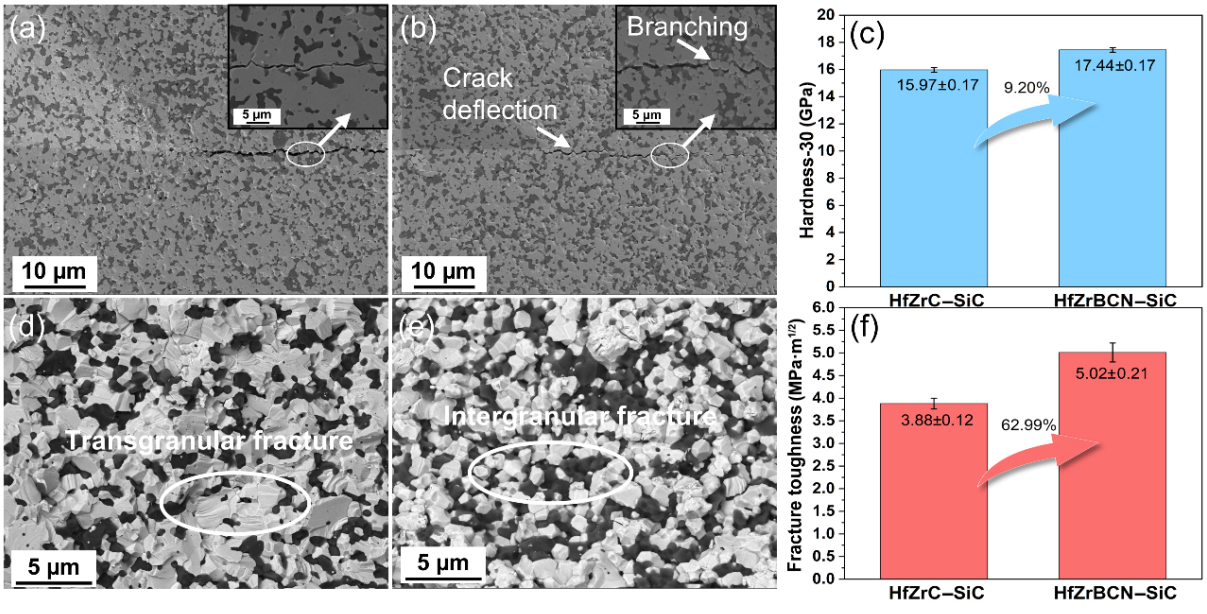

Fig. 2 Vickers indentation crack propagation paths in (a) HfZrC–SiC and (b) HfZrBCN–SiC (insets display high-magnification views of crack tips); comparison of (c) Vickers hardness and (f) fracture toughness of HfZC–SiC and HfZrBCN–SiC ceramics; Representative fracture surface morphologies of (d) HfZrC–SiC and (e) HfZrBCN–SiC.

a liquid binder, consolidating solid particles and filling cracks. Some small $HfZrO_2$ particles dispersed in SiO_2 pin the liquid phase, increasing the viscosity and suppressing volatilization [58]. However, distinct microstructural differences indicate divergent protective mechanisms. For the HfZrC–SiC composite (Figs. 4(b)–4(d)), severe surface degradation is evident. At the ablation center (Fig. 4(b)), extensive liquid phase spattering is observed. In the transition area (Fig. 4(c)) and at the edge (Fig. 4(d)), numerous broken bubbles are observed throughout the oxide scale, indicating poor structural integrity of the oxide layer. In contrast, the HfZrBCN–SiC ceramic (Figs. 4(f)–4(h)) exhibits a markedly different morphology with a relatively intact oxide layer. Specifically, the surface shows almost no liquid phase spattering and only a few bubbles in the transition area (Fig. 4(g)).

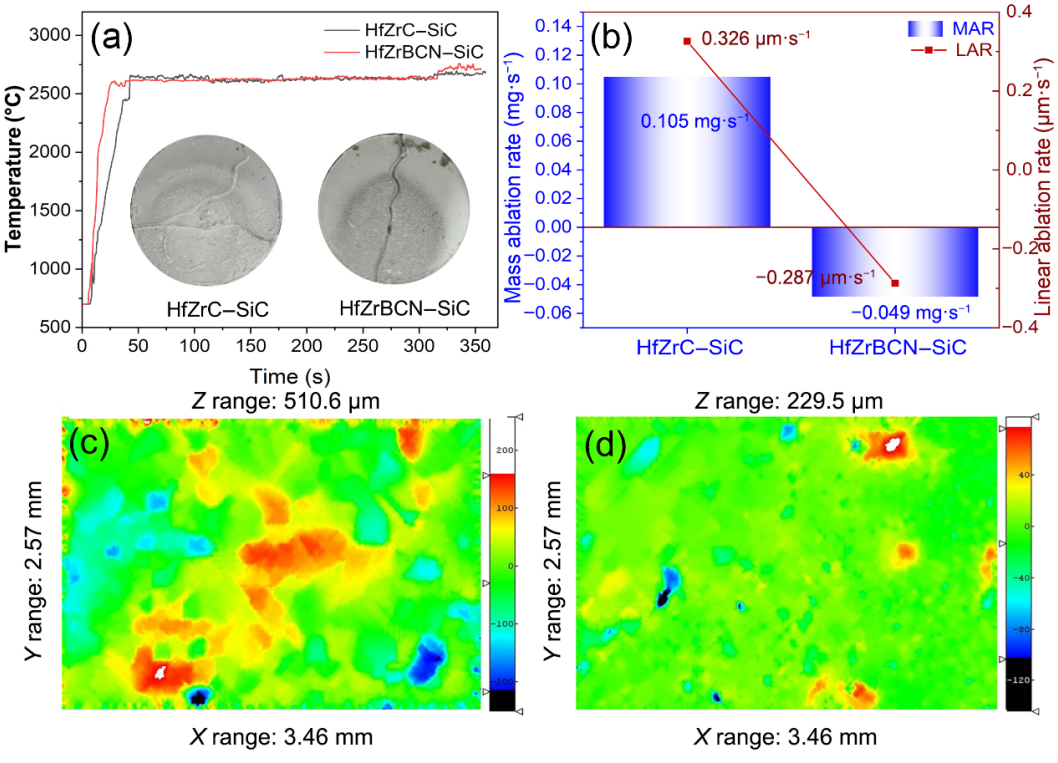

Fig. 3 (a) Surface response temperature of HfZrC–SiC and HfZrBCN–SiC ceramics as a function of ablation time. Inserts are macromorphologies of ceramics after ablation; (b) linear and mass ablation rates of HfZrC–SiC and HfZrBCN–SiC ceramics ablated at 2600 °C for 300 s; 3D surface morphology of (c) HfZrC–SiC and (d) HfZrBCN–SiC ceramics after ablation.

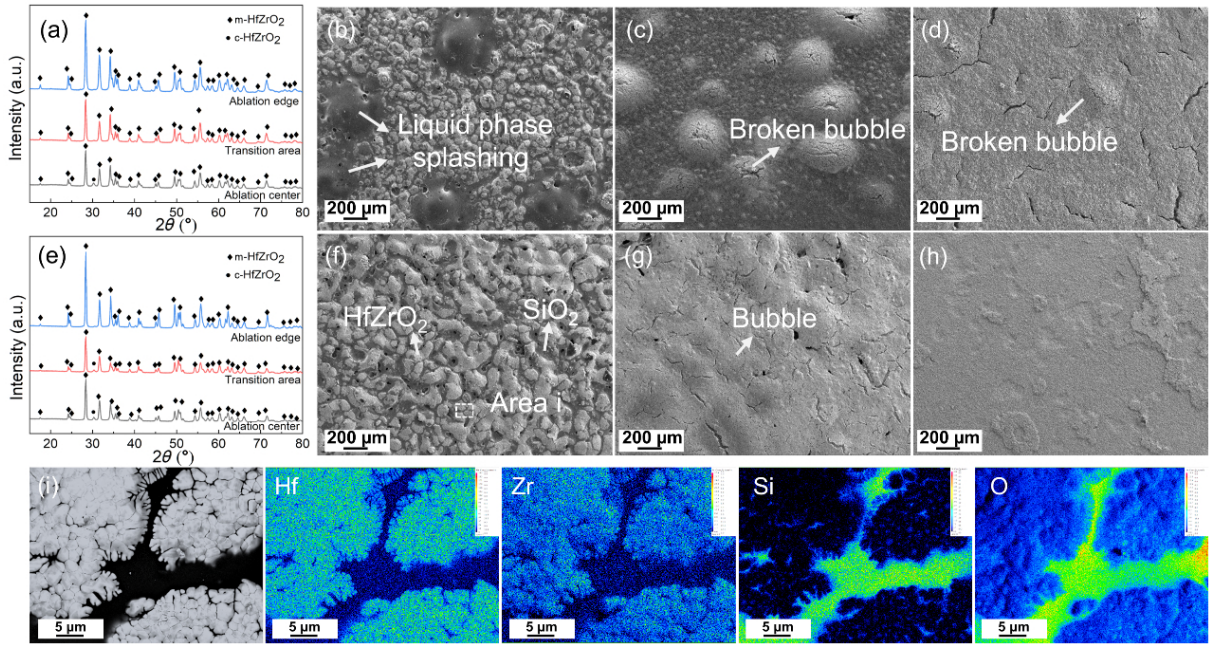

Fig. 4 XRD patterns of (a) HfZrC–SiC and (e) HfZrBCN–SiC at ablation center, transition area, and edge; SEM micrographs of (b–d) HfZrC–SiC and (f–h) HfZrBCN–SiC showing (b, f) ablation center, (c, g) transition area, and (d, h) ablation edge; (i) EPMA elemental mapping of Hf, Zr, Si, and O at HfZrBCN–SiC ablation center.

Figure 5 presents cross-sectional XRD and EPMA analyses, revealing markedly distinct oxygen penetration behaviors and phase evolution in the two ceramics during ablation. For HfZrC–SiC, EPMA elemental mapping reveals a four-layer structure dictated by the oxygen concentration gradient (Fig. 5(b)). The deepest region is the unoxidized base layer, retaining pristine HfZrC and SiC phases. Above it, an interlayer forms comprising HfZrCO oxycarbide (structurally similar to HfZrC) intermixed with residual SiC. Proximal to the surface, the oxygen content rises sharply, SiC undergoes severe active oxidation ($SiC + O_2 \rightarrow SiO\uparrow + CO\uparrow$), forming a SiC-depleted layer characterized by significantly weakened HfZrCO diffraction peaks concurrent with the emergence of $HfZrO_2$. At the outermost surface, HfZrCO is completely oxidized to $HfZrO_2$. Notably, the oxide layer of HfZrC–SiC exhibits an elevated silicon content and severe surface damage characterized by numerous ruptured bubbles and liquid spattering (Figs. 4(b)–4(d)). This degradation stems from the active oxidation of SiC in the underlying depletion layer, which generates substantial SiO gas. The continuous evolution of SiO gas disrupts the oxide skeleton, causing structural collapse and pore proliferation, thereby forming the observed bubbles (Figs. 4(c) and 4(d)). Upon reaching the surface, SiO further oxidizes to form low-viscosity SiO_2, which is easily scoured by high-speed gas flow, leading to liquid spattering (Fig. 4(b)) [59].

In stark contrast, HfZrBCN–SiC exhibits a markedly different three-layer structure comprising a base layer, a dense interlayer, and a surface oxide layer, with no detectable SiC depletion layer (Figs. 5(c) and 5(d)). XRD analysis reveals that while the oxide layer also consists of $HfZrO_2$, the underlying interlayer retains substantial partially oxidized HfZrBCNO and SiC, indicating significantly suppressed oxidation. To gain deeper insight into the structure and composition of these critical transition zones, FIB samples were extracted from the base layer–interlayer and interlayer–oxide layer interfaces (marked as FIB_1 and FIB_2 in Fig. 5(d)) for detailed TEM analysis.

3.3 Mechanisms underlying superior ablation-resistant performance

To elucidate the microstructural characteristics at the interlayer–base layer transition zone in HfZrBCN–SiC, systematic TEM analysis was performed on the FIB_1 sample (Fig. 6). The low-magnification high-angle annular dark-field (HAADF) image (Fig. 6(a)) reveals a distinct boundary morphology: The base layer comprises equiaxed dark and bright grains, whereas the interlayer exhibits elongated grains with alternating contrast. Combined EDS mapping (Fig. 6(d)) and SAED patterns (Figs. 6(b1) and 6(b2)) identify the base layer phases as FCC HfZrBCN and SiC.

HRTEM analysis (Fig. 6(c)) together with fast Fourier transform (FFT)/inverse fast Fourier transform (IFFT) analyses and EDS mapping (Fig. 6(d)) reveal that the interlayer consists of hexagonal graphite precipitates and HfZrBCNO. Notably, the dark SiC grains show no evidence of oxidation. The formation of this distinctive interlayer structure originates from the competitive oxidation behavior between the HfZrBCN matrix and SiC reinforcements under limited oxygen supply conditions. Due to the higher oxygen affinity of the multianion HfZrBCN solid solution relative to SiC, the inward-diffusing oxygen preferentially attacks the HfZrBCN phase, penetrating along grain boundaries into the grain interiors to form a metastable HfZrBCNO solid solution. As oxygen dissolves into the anion sublattice, carbon atoms are displaced from their original lattice positions to accommodate oxygen incorporation. The precipitation of solid graphite rather than gaseous CO/CO_2 in the interlayer arises from the limited local oxygen partial pressure. Similar thermodynamic behavior has been reported in multicomponent Hf–Zr–Ti–C systems, where preferential oxidation of Hf and Zr consumes the available oxygen, creating a local environment where carbon is expelled from the lattice yet remains thermodynamically stable as hexagonal graphite within the carbon-bearing oxide interlayer [60]. Consequently, the displaced carbon precipitates *in situ* as hexagonal graphite, resulting in the characteristic elongated, alternating morphology of HfZrBCNO grains and graphite precipitates. Meanwhile, the SiC grains remain pristine and unoxidized because the surrounding HfZrBCN matrix effectively acts as an oxygen scavenger, consuming the available oxygen before it reaches the SiC interfaces.

Furthermore, geometric phase analysis (GPA) strain mapping was employed to elucidate the multiscale toughening mechanisms in the hexagonal graphite/HfZrBCNO region (Fig. 6(e)). At the microscopic scale, the graphite region exhibits a high-amplitude, heterogeneous strain distribution, corresponding to nonuniform deformation of the wrinkled structure. In contrast, the HfZrBCNO ceramic region displays relatively low strain (< 0.2) with regular banding patterns, indicating elastic load-bearing behavior. In particular, the hexagonal graphite/HfZrBCNO

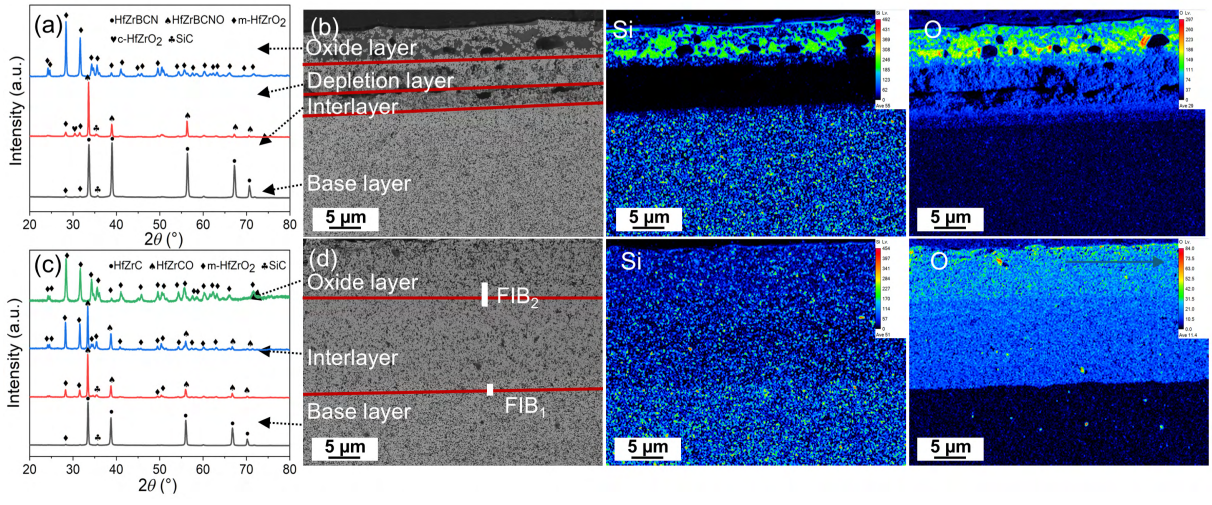

Fig. 5 XRD patterns of (a) HfZrC–SiC and (c) HfZrBCN–SiC at different depths after ablation; cross-sectional SEM images with corresponding EPMA elemental mappings (Si and O) of (b) HfZrC–SiC and (d) HfZrBCN–SiC.

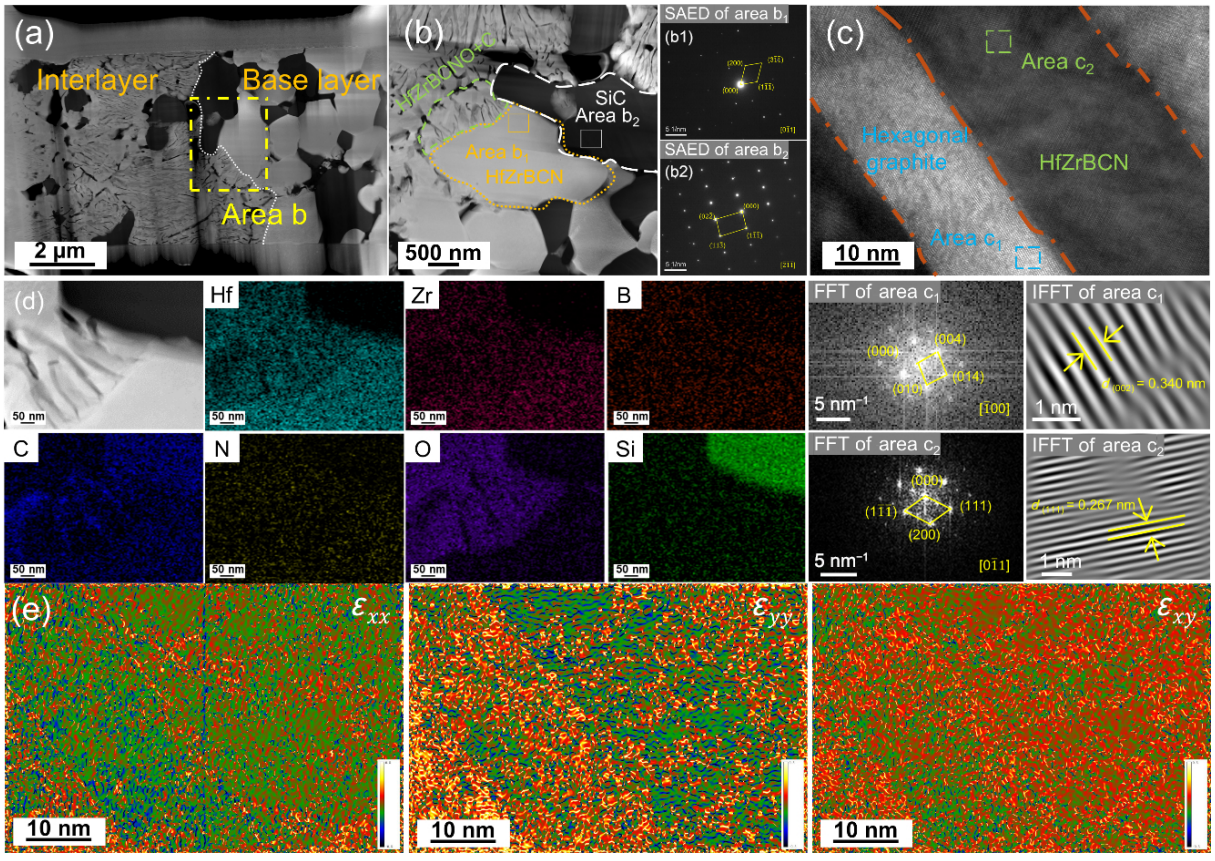

Fig. 6 (a) HAADF overview of interlayer and base layer regions (FIB_1); (b) HAADF image of area b (in (a)) with corresponding SAED patterns (insets) of (b1) HfZrBCN (area b_1) and (b2) SiC (area b_2); (c) HRTEM of hexagonal graphite precipitates within HfZrBCNO matrix (areas c_1 and c_2) with FFT and IFFT analyses; (d) EDS elemental mapping (Hf, Zr, B, C, N, O, and Si) across transition region from interlayer to base layer; (e) GPA strain maps (ε_{xx}, ε_{yy}, and ε_{xy}) of hexagonal graphite precipitates within HfZrBCNO.

interface region shows a significant shear strain concentration ($\varepsilon_{xy} \approx \pm 0.5$), suggesting that the soft graphite phase dissipates fracture energy through interfacial shear deformation [61]. This extrinsic toughening via load transfer, crack deflection, and bridging effects of hexagonal graphite, coupled with the intrinsically elevated fracture toughness arising from anion sublattice engineering, synergistically enhances the damage tolerance of the composite. Consequently, unlike the inherently brittle HfZrC–SiC, the HfZrBCN–SiC ceramic does not undergo complete fragmentation under severe thermal shock.

Figure 7 presents a systematic TEM characterization of the microstructural evolution from the interlayer to the oxide scale in HfZrBCN–SiC (FIB_2). The low-magnification HAADF image (Fig. 7(a)) reveals a distinct oxide layer and interlayer regions: The left side shows the outer oxide layer composed of large grains, while the right side presents a dense interlayer consisting of fine grains. Two representative areas were selected for further high-resolution characterization.

Figure 7(b) presents the HAADF image and corresponding EDS mapping of zone i. The bright grains are HfZrBCNO, and the dark grains are unoxidized SiC. HRTEM analysis of B- and N-enriched zones confirms h-BN (Fig. 7(b)). Notably, HfZrBCNO grains exhibit a morphological transition from elongated in deeper regions to fine equiaxed in this zone, accompanied by graphite consumption. The continuous HfZrBCNO matrix encapsulates and protects SiC particles. This consumption stems from the progressive oxidation of the interlayer as the oxidation front advances. In the deeper interlayer region (FIB_1, Fig. 6), the local oxygen partial pressure is sufficiently low that carbon expelled from the HfZrBCN lattice precipitates as stable hexagonal graphite rather than being oxidized to gaseous CO/CO_2. However, as the oxidation front progresses toward the surface into this intermediate zone (FIB_2), the local oxygen activity increases concomitantly. The previously precipitated graphite undergoes partial oxidation upon exposure to the higher oxygen flux, generating CO and CO_2 that volatilize and escape from the interlayer. This graphite depletion drives the morphological transition of HfZrBCNO grains from elongated (graphite-interspersed) to fine equiaxed (graphite-free) grains. Meanwhile, as oxygen continues to penetrate inward from the outer oxide scale, continued substitution into the anion sublattice progressively destabilizes boron and nitrogen within the HfZrBCNO lattice. These expelled B and N atoms migrate along grain boundaries and precipitate as hexagonal BN (h-BN), as confirmed by HRTEM analysis of the B- and N-enriched zones (Fig. 7(b1)). Unlike the graphite consumed in the deeper interlayer, this h-BN persists owing to its superior oxidation resistance [62–64]. Furthermore, the persistence of both *h*-BN and the metastable HfZrBCNO interlayer under such extreme thermal conditions reflects the enhanced thermal stability conferred by nitrogen in the anion sublattice. *Ab initio* molecular dynamics calculations by Hong *et al.* [36] identified $HfC_{0.75}N_{0.22}$ as the highest-melting compound known (~4400 K), attributing this to nitrogen-induced stabilization of the solid phase relative to the liquid. This theoretical prediction aligns with our experimental observation that the HfZrBCNO interlayer remains structurally intact even in regions proximal to the oxide layer, forming a continuous, dense barrier that encapsulates and protects SiC particles. The minor *h*-BN precipitation at grain boundaries serves a dual function. First, it acts as a compliant thermal expansion

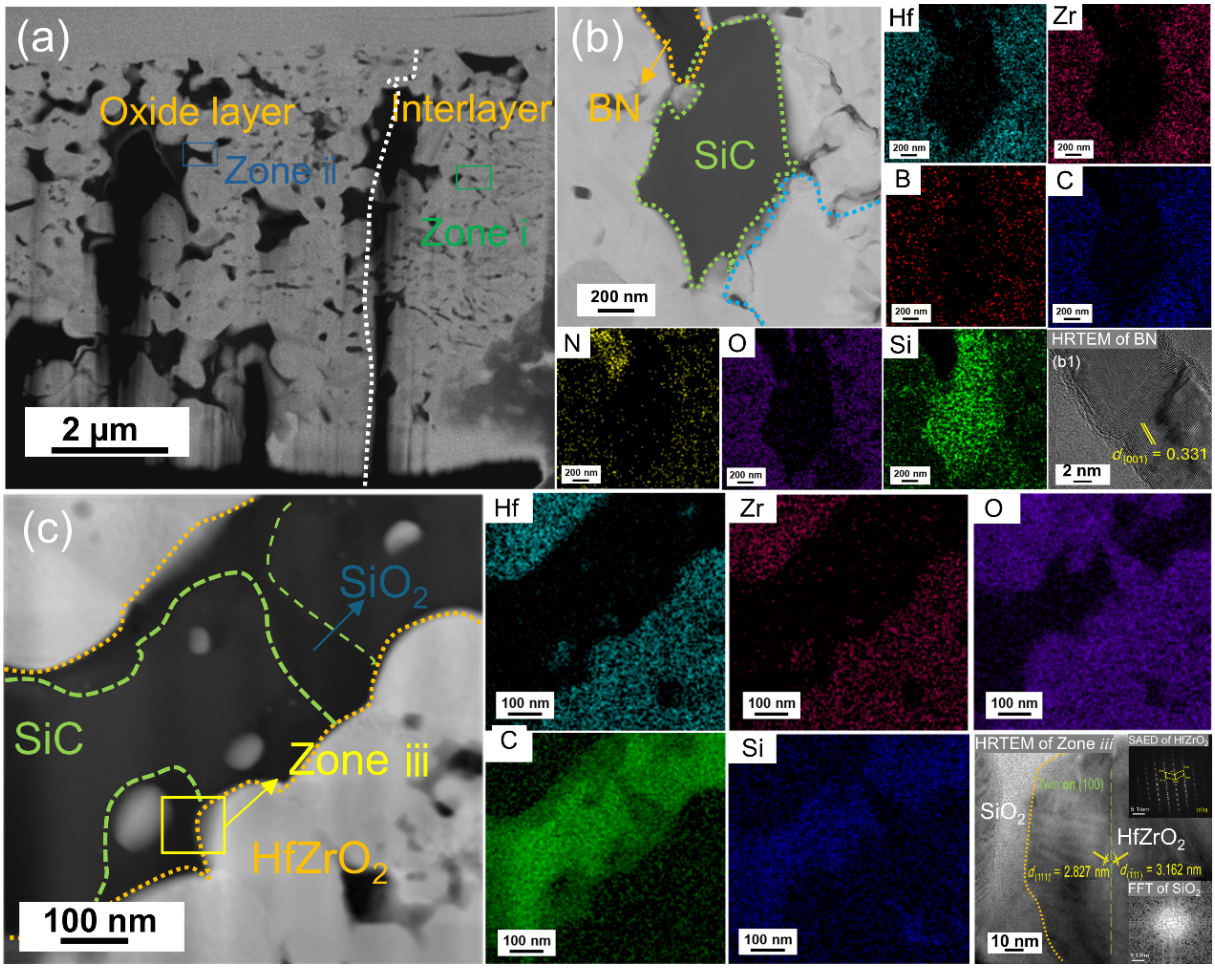

Fig. 7 (a) HAADF overview of oxide layer and interlayer regions; (b) EDS mapping of zone i and (b1) HRTEM of BN; (c) EDS mapping of zone ii and HRTEM of zone iii.

buffer, accommodating dimensional changes through elastic deformation to alleviate the CTE mismatch between rigid SiC and the matrix. Second, it functions as a physical diffusion barrier, hindering oxygen ingress toward SiC grain boundaries.

Figure 7(c) presents the further analysis of zone ii. HfZrBCNO is completely oxidized to large $HfZrO_2$ particles. The SiC particle surface is covered with a continuous SiO_2 oxide film, with some small $HfZrO_2$ particles dissolved within the SiO_2 glass phase. HRTEM analysis confirms that SiO_2 is amorphous, while $HfZrO_2$ exhibits a twinned structure (HRTEM of zone iii). This is attributed to the rapid cooling, which does not allow sufficient time for the complete release of phase transformation stress in $HfZrO_2$. Notably, the passive oxidation of SiC to SiO_2 is confined to the outermost oxide layer (Fig. 7(c)), where the oxygen partial pressure is sufficiently high; in the underlying dense interlayer, SiC remains pristine and protected.

Figure 8 presents a schematic illustration contrasting the ablation behaviors of HfZrC–SiC and HfZrBCN–SiC under a plasma flame at 2600 °C, revealing the multiscale protective mechanisms conferred by the B–C–N solid solution. As depicted in Fig. 8(a), HfZrC–SiC exhibits catastrophic failure during ablation. Active oxidation of SiC ($SiC + O_2 \rightarrow SiO\uparrow + CO\uparrow$) generates substantial gaseous products, forming a loose, porous SiC-depleted layer. At the surface with high oxygen partial pressure, SiO(g) reoxidizes to form abundant liquid SiO_2 with low viscosity at 2600 °C, which splashes under high-velocity gas scouring. Consequently, the resulting oxide layer is rough and porous and unable to withstand thermal stresses, which initiates cracks. Due to the presence of a porous SiC-depleted layer and the coarse grain structure, cracks rapidly propagate inward, leading to severe fragmentation. In stark contrast, HfZrBCN–SiC (Fig. 8(b)) demonstrates exceptional ablation resistance. No active oxidation of SiC occurs beneath the surface, and the oxide layer remains dense and intact. The ablated ceramic merely fractures into two halves without catastrophic disintegration.

Figures 8(b1)–8(b5) schematically illustrate the sequential phase transformations in HfZrBCN–SiC from the pristine substrate to the outer oxide layer. Deep within the substrate (Fig. 8(b1)), the material retains its original microstructure comprising a fine-grained HfZrBCN solid solution with uniformly dispersed SiC grains. Compared with the coarse-grained HfZrC–SiC counterpart, the fine grain size provides enhanced fracture toughness. As oxygen penetrates inward, HfZrBCN grains oxidize to form striped HfZrBCNO and graphite precipitates (Fig. 8(b2)). The hexagonal graphite particles, with their characteristic layered structure, act as compliant second-phase inclusions that effectively dissipate fracture energy through crack deflection and interfacial shear, fundamentally enhancing the material's thermal shock resistance. Concurrently, early-stage oxidation of the HfZrBCN matrix consumes the inward-diffusing oxygen, enabling SiC to retain its protected pristine state.

Further toward the oxide layer (Fig. 8(b3)), where the oxygen content increases, the elongated HfZrBCNO grains transform into fine equiaxed grains. These HfZrBCNO grains exhibit excellent oxidation resistance and remain unoxidized even in regions close to the oxide layer, forming a continuous, dense barrier that

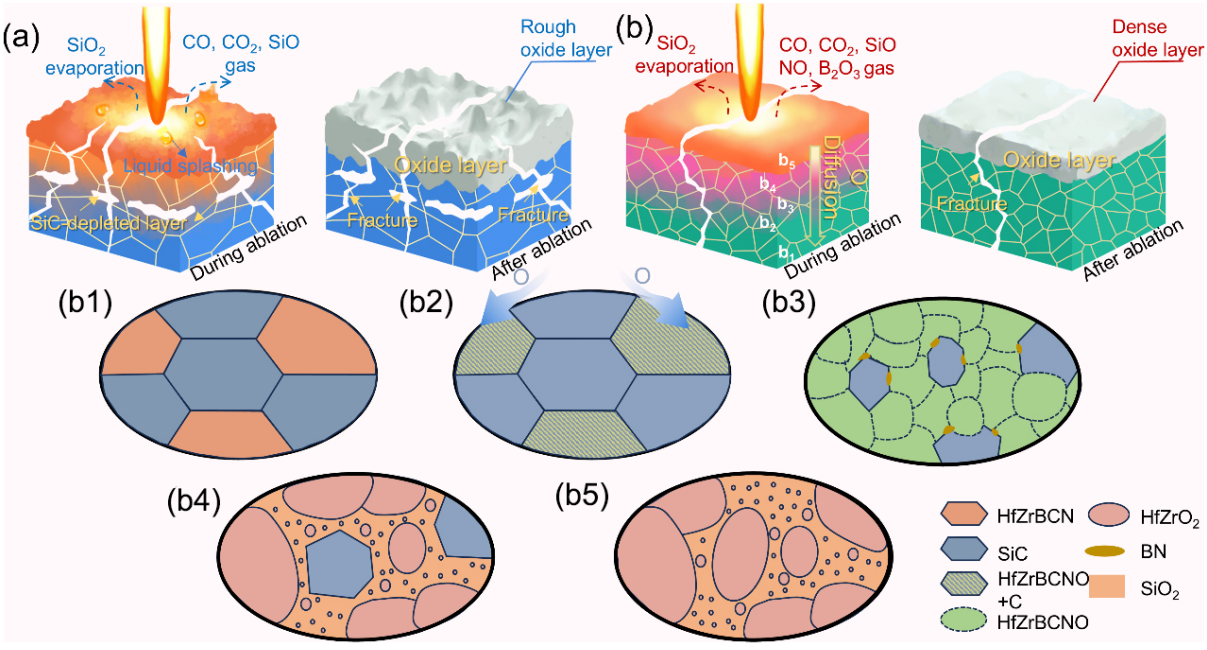

Fig. 8 Schematic illustration of ablation mechanisms and microstructural evolution in (a) HfZrC–SiC and (b) HfZrBCN–SiC ceramics under a plasma flame at 2600 °C; (b1–b5) microstructural evolution of HfZrBCN–SiC from base layer to fully oxidized layer: (b1) original HfZrBCN matrix with SiC grains; (b2) HfZrBCNO formation with C precipitation; (b3) partial oxidation with BN precipitation; (b4) complete oxidation of HfZrBCN to $HfZrO_2$ with residual SiC; (b5) oxidation of SiC to SiO_2 glass phase, forming a dense composite oxide layer on outer surface.

encapsulates the SiC particles. Simultaneously, *h*-BN precipitates at grain boundaries, serving as a compliant thermal expansion buffer that alleviates the coefficient of thermal expansion (CTE) mismatch between the rigid SiC grains and the ceramic matrix [65]. More importantly, the continuous *h*-BN networks act as effective diffusion barriers, physically blocking oxygen ingress into SiC.

In the outermost oxide layer (Figs. 8(b4) and 8(b5)), HfZrBCNO is completely oxidized to large $HfZrO_2$ particles. SiC in this region undergoes passive oxidation to form the SiO_2 glass phase. The limited SiO_2 melt does not splash. Instead, it infiltrates the porous $HfZrO_2$ skeleton, fills intergranular voids and pins $HfZrO_2$ grains, forming a dense and well-bonded $HfZrO_2$–SiO_2 composite layer. Furthermore, small $HfZrO_2$ particles dissolve into the glass phase, increasing viscosity and preventing volatilization. These mechanisms collectively yield a negative linear ablation rate ($-0.287\ \mu m \cdot s^{-1}$) and mass ablation rate ($-0.049\ mg \cdot s^{-1}$), indicating that oxide growth exceeds material loss.

4 Conclusions

In summary, we have developed a multianion HfZrBCN–SiC ceramic demonstrating exceptional ablation resistance at 2600 °C with negative ablation rates. The multianion entropy engineering achieves hierarchical protection through:

(1) Microscale toughening: The incorporation of B–C–N intrinsically enhances fracture toughness through combined bond weakening (lower energy M–N bonds replacing rigid M–C bonds for local deformability) and sluggish diffusion-induced grain refinement that promotes intergranular fracture and crack deflection. Concurrently, *in situ* precipitated hexagonal graphite during ablation acts as a compliant second phase that extrinsically arrests cracks through interfacial shear, effectively dissipating fracture energy and preventing catastrophic disintegration under severe thermal shock.

(2) Mesoscale oxidation management: Synergistic formation of HfZrBCNO (oxygen scavenging) and h-BN (diffusion blocking) at grain boundaries creates a dense interlayer that suppresses the active oxidation of SiC, eliminating the porous SiC-depleted layers observed in conventional HfZrC–SiC. This facilitates the formation of a dense $HfZrO_2$–SiO_2 composite barrier with high viscosity that withstands high-velocity gas scouring.

By demonstrating simultaneous microstructural toughening and mesoscale oxidation management, this work establishes multianion sublattice engineering as a transformative platform. This paradigm provides a versatile compositional strategy for developing advanced ceramics capable of withstanding extreme aerothermal environments in hypersonic flight and aerospace thermal protection systems.

Acknowledgements

The financial support from the National Natural Science Foundation of China (Nos. 52472114, 52332003, 52402135, and 52502084), the Program of Shanghai Academic/Technology Research Leader (No. 23XD1424300), and the Postdoctoral Fellowship Program (Grade B) of China Postdoctoral Science Foundation (No. GZB20240786) are greatly acknowledged.

Author contributions

Xiaoyu Wang: conceptualization, methodology, analysis, writing – review and editing, and investigation. Dewei Ni: funding acquisition, writing – review and editing, and investigation. Bowen Chen: investigation and conceptualization. Feiyan Cai: funding acquisition, validation, and conceptualization. Yang Hu: investigation and conceptualization. Yanmei Kan: methodology and investigation. Yusheng Ding: writing – review and editing. Shaoming Dong: writing – review and editing and supervision.

Availability of data and materials

The data that support the findings of this study are available from the corresponding author upon reasonable request.

Competing interests

The authors have no competing interests to declare that are relevant to the content of this article. The author Dewei Ni is the Editorial Committee member of this journal.

References

[1] Yang YZ, Yang JL, Fang DN. Research progress on thermal protection materials and structures of hypersonic vehicles. *Appl Math Mech-Engl* 2008, **29**: 51–60.

[2] Mungiguerra S, Di Martino GD, Cecere A, *et al.* Ultra-high-temperature testing of sintered ZrB_2-based ceramic composites in atmospheric re-entry environment. *Int J Heat Mass Tran* 2020, **156**: 119910.

[3] Parthasarathy TA, Petry MD, Cinibulk MK, *et al.* Thermal and oxidation response of UHTCL eading edge samples exposed to simulated hypersonic flight conditions. *J Am Ceram Soc* 2013, **96**: 907–915.

[4] Fahrenholtz WG, Hilmas GE. Ultra-high temperature ceramics: Materials for extreme environments. *Scripta Mater* 2017, **129**: 94–99.

[5] Savino R, Criscuolo L, Di Martino GD, *et al.* Aero-thermo-chemical characterization of ultra-high-temperature ceramics for aerospace applications. *J Eur Ceram Soc* 2018, **38**: 2937–2953.

[6] Guo LW, Liu JX, Qin Y, *et al.* The indentation load effect of hardness of non-stoichiometric high-entropy carbides $(Ti_{0.2}Zr_{0.2}Hf_{0.2}Nb_{0.2}Ta_{0.2})C_{1-x}$. *Adv Ceram* 2024, **45**: 169–176. (in Chinese)

[7] Zhang XH, Wang YM, Cheng Y, *et al.* Research progress on ultra-high temperature ceramic composites. *J Inorg Mater* 2024, **39**: 571–590.

[8] Justin JF, Julian-Jankowiak A, Guérineau V, *et al.* Ultra-high temperature ceramics developments for hypersonic applications. *CEAS Aeronaut J* 2020, **11**: 651–664.

[9] Ni DW, Cheng Y, Zhang JP, *et al.* Advances in ultra-high temperature ceramics, composites, and coatings. *J Adv Ceram* 2022, **11**: 1–56.

[10] Monteverde F, Bellosi A, Scatteia L. Processing and properties of ultra-high temperature ceramics for space applications. *Mat Sci Eng A—Struct* 2008, **485**: 415–421.

[11] Zhao T, Liu JX, Xu YX, *et al.* The effect of SiC on the laser ablation resistance of high-entropy diboride ceramics. *Adv Ceram* 2024, **45**: 417–433. (in Chinese)

[12] Ping H, Wang GL, Zhi W. Oxidation mechanism and resistance of ZrB_2–SiC composites. *Corros Sci* 2009, **51**: 2724–2732.

[13] Hao W, Lu XZ, Li L, *et al.* Toughened $(Ti_{0.2}Zr_{0.2}Hf_{0.2}Nb_{0.2}Ta_{0.2})B_2$–SiC composites fabricated by one-step reactive sintering with a unique SiB_6 additive. *J Adv Ceram* 2024, **13**: 86–100.

[14] Guo LX, Dong YJ, Wang YQ, *et al.* Ablation behavior of Hf–Zr-modified silicon-based ceramic coatings prepared by polymer derived ceramics and gaseous silicon infiltration. *Chinese J Aeronaut* 2026, **39**: 104010.

[15] Chamberlain AL, Fahrenholtz WG, Hilmas GE, *et al.* High-strength zirconium diboride-based ceramics. *J Am Ceram Soc* 2004, **87**: 1170–1172.

[16] Chen ZZ, Liu LP, Guo J, *et al.* Oxidation behavior of SiC in dissociated oxygen environments. *Acta Mater* 2025, **286**: 120745.

[17] Ren Y, Qian YH, Xu JJ, *et al.* Oxidation resistance and microstructure evolution of ZrB_2–SiC–La_2O_3/SiC dual-layer coating on siliconized graphite at 1800 °C under low air pressures. *Ceram Int* 2020, **46**: 27150–27157.

[18] Zhang XH, Hu P, Han JC. Structure evolution of ZrB_2–SiC during the oxidation in air. *J Mater Res* 2008, **23**: 1961–1972.

[19] Le Maout V, Yang Y, You H, *et al.* A numerical oxidation model for SiC-coated thermal protection systems in hypersonic applications. *J Am Ceram Soc* 2024, **107**: 7237–7252.

[20] Zhou SG, Li RZ, Liu X, *et al.* Modeling of oxidation resistance characteristics of silicon carbide/zirconium diboride ultra-high temperature ceramics. *Acta Aerodyn Sin* 2025, **43**: 73–82.

[21] Han JC, Hu P, Zhang XH, *et al.* Oxidation-resistant ZrB_2–SiC composites at 2200 °C. *Compos Sci Technol* 2024, **68**: 799–806.

[22] Gao W, Wang XG, Wang XF, *et al.* Preparation of $(Ti,Zr,Hf)B_2$ powders and effect of B_4C content on the high temperature flexural strength of medium entropy ceramics. *Adv Ceram* 2023, **44**: 342–351. (in Chinese)

[23] Cai FY, Ni DW, Dong SM. Research progress of high-entropy carbide ultra-high temperature ceramics. *J Inorg Mater* 2024, **39**: 591–608. (in Chinese)

[24] Li JC, Lu FY, Li T, *et al.* Superior synergistic oxidation resistance of medium-entropy carbide ceramic powders rather than multi-phase carbide ceramic powders. *J Adv Ceram* 2024, **13**: 1223–1233.

[25] Hsu WL, Tsai CW, Yeh AC, *et al.* Clarifying the four core effects of high-entropy materials. *Nat Rev Chem* 2024, **8**: 471–485.

[26] Yan Z, Liu J, Peng P, *et al.* Oxidation resistance of equimolar multicomponent transition metal carbide solid solution. *Adv Ceram* 2024, **45**: 541–557. (in Chinese)

[27] Li JC, Zhang YL, Zhao YX, *et al.* A novel $(Hf_{1/3}Zr_{1/3}Ti_{1/3})C$ medium-entropy carbide coating with excellent long-life ablation resistance applied above 2100 °C. *Compos Part B—Eng* 2023, **251**: 110467.

[28] Chu YH, Yu HL, Liu YW, *et al.* Melting points of metal oxides. *Adv Funct Mater* 2026, **36**: 74823.

[29] Huang KJ, Han XC. High-temperature oxidation properties of Ti–Hf–Mo–Ta–Nb–B composite coating deposited on Ti60 alloy with laser cladding. *Coatings* 2023, **13**: 1646.

[30] Chen SY, Chen ZK, Song WL, *et al.* Formation mechanism and microstructural evolution of bubbles during ultra-high temperature oxidation of multicomponent carbides. *J Mater Sci Technol* 2025, **236**: 122–135.

[31] Song GM, Li SB, Zhao CX, *et al.* Ultra-high temperature ablation behavior of Ti_2AlC ceramics under an oxyacetylene flame. *J Eur Ceram Soc* 2011, **31**: 855–862.

[32] Zeng Y, Wang DN, Xiong X, *et al.* Ablation-resistant carbide $Zr_{0.8}Ti_{0.2}C_{0.74}B_{0.26}$ for oxidizing environments up to 3000 °C. *Nat Commun* 2017, **8**: 15836.

[33] Lun HL, Zeng Y, Xiong X, *et al.* Oxidation behavior of boron-containing $(Zr,Ti)C_xB_y$ solid solution ceramics at 1600 °C in air. *J Adv Ceram* 2023, **12**: 1989–2002.

[34] Peng Z, Ma QS, Cui YJ, *et al.* Tailored $C_{sf}/HfC_{0.76}N_{0.24}$ composites for superior ablation resistance at 3000°C. *Adv Powder Mater* 2025, **4**: 100281.

[35] Wyatt BC, Nemani SK, Hilmas GE, *et al.* Ultra-high temperature ceramics for extreme environments. *Nat Rev Mater* 2024, **9**: 773–789.

[36] Hong QJ, van de Walle A. Prediction of the material with highest known melting point from *ab initio* molecular dynamics calculations. *Phys Rev B* 2015, **92**: 020104.

[37] Peng Z, Sun W, Xiong X, *et al.* Novel nitrogen-doped hafnium carbides for advanced ablation resistance up to 3273 K. *Corros Sci* 2021, **189**: 109623.

[38] Wu J, Ma XS, Zhou DH, *et al.* High-entropy high-temperature high-piezoelectricity ceramics. *Adv Mater* 2025, **37**: 2419134.

[39] Guan JY, Li DX, Yang ZH, *et al.* Ta(B,C,N) and (Ta,Mi)(B,C,N) (Mi = Nb, W) ceramics by high-energy ball milling: Processing and solution mechanisms. *J Am Ceram Soc* 2023, **106**: 699–708.

[40] Guan JY, Li DX, Yang ZH, *et al.* Synthesis and thermal stability of novel high-entropy metal boron carbonitride ceramic powders. *Ceram Int* 2020, **46**: 26581–26589.

[41] Guan JY, Liu YC, Li DX, *et al.* The new complex high-entropy metal boron carbonitride: Microstructure and mechanical properties. *J Am Ceram Soc* 2022, **105**: 6417–6426.

[42] Lun HL, Zeng Y, Xiong X, *et al.* Novel solid-state diffusion strategy for fabricating boron/nitrogen-containing ternary-anion (Zr,Hf,Ti)(C,B,N) carbide with enhanced oxidation resistance. *Ceram Int* 2025, **51**: 66168–66174.

[43] Wang XY, Ni DW, Chen BW, *et al.* Synthesis of novel multi-anion $Hf_{0.8}Zr_{0.2}B_{0.1}C_{0.5}N_{0.4}$ powder. *J Am Ceram Soc* 2025, **108**: 70218.

[44] Dippo OF, Vecchio KS. A universal configurational entropy metric for high-entropy materials. *Scripta Mater* 2021, **201**: 113974.
[45] Guo LX, Huang SW, Li W, *et al.* Theoretical design and experimental verification of high-entropy carbide ablative resistant coating. *Adv Powder Mater* 2024, **3**: 100213.
[46] Xia LS, Hu PT, Dong S, *et al.* Enhancing the mechanical properties and oxidation resistance of high-entropy $(Ti_{0.2}Zr_{0.2}Hf_{0.2}Nb_{0.2}Ta_{0.2})C_{0.95}$ ceramics through nitrogen doping. *J Mater Sci Technol* 2025, **235**: 12–27.
[47] Zhang P, Liu XJ, Cai AH, *et al.* High-entropy carbide-nitrides with enhanced toughness and sinterability. *Sci China Mater* 2021, **64**: 2037–2044.
[48] Lu Y, Sun YN, Zhang TZ, *et al.* Polymer-derived Ta_4HfC_5 nanoscale ultrahigh-temperature ceramics: Synthesis, microstructure and properties. *J Eur Ceram Soc* 2019, **39**: 205–211.
[49] Lengauer W, Binder S, Aigner K, *et al.* Solid state properties of group IVb carbonitrides. *J Alloy Compd* 1995, **217**: 137–147.
[50] Wang YC, Csanádi T, Zhang HF, *et al.* Synthesis, microstructure, and mechanical properties of novel high entropy carbonitrides. *Acta Mater* 2022, **231**: 117887.
[51] Wang HY, Bi JQ, Yang Y, *et al.* Preparation, characterization and performance of high-entropy carbonitride ceramics. *Ceram Int* 2024, **50**: 3034–3040.
[52] Liu Y, Ma SQ, Wang TY, *et al.* Preparation, microstructure and mechanical properties of novel WC–(Ti,Ta,Mo,V,Cr)(C,N)–Co high-entropy composites. *Mater Charact* 2024, **212**: 113997.
[53] Chen ZH, Zhang W, Fu FW, *et al.* Influence of carbon content on the microstructural evolution and mechanical properties of $(TiZrHfNbTaCr)C_x$ carbides. *J Am Ceram Soc* 2026, **109**: 70735.
[54] Xie W, Zhang ZL, Zhao ZQ, *et al.* Microstructure and high-temperature tribological properties of medium-entropy $(Ti_{1/3}Zr_{1/3}Ta_{1/3})(B_{1.6}C_{0.4})$ ceramic. *Tribol Int* 2026, **213**: 111095.
[55] Mei ZG, Bhattacharya S, Yacout AM. First-principles study of fracture toughness enhancement in transition metal nitrides. *Surf Coat Tech* 2019, **357**: 903–909.
[56] Zhang XT, Li XC, Zuo J, *et al.* Characterization of thermophysical and mechanical properties of hafnium carbonitride fabricated by hot pressing sintering. *J Mater Res Technol* 2023, **23**: 4432–4443.
[57] Shen TZ, Li CY, Ouyang HB, *et al.* A facile fine-grain strategy to fabricate $(Ta_{0.2}Nb_{0.2}Ti_{0.2}Hf_{0.2}Zr_{0.2})C$–SiC ceramics with enhanced strength and toughness. *Mat Sci Eng A—Struct* 2025, **929**: 148125.
[58] Chen BW, Ni DW, Bao WC, *et al.* Engineering C_f/ZrB_2–SiC–Y_2O_3 for thermal structures of hypersonic vehicles with excellent long-term ultrahigh temperature ablation resistance. *Adv Sci* 2023, **10**: 2304254.
[59] Wu DJ, Cai XT, Qin X, *et al.* Laser ablation behavior and mechanism of C_f/C–SiC composites under different laser energy densities. *Compos Part B—Eng* 2024, **276**: 111359.
[60] Ye ZM, Zeng Y, Xiong X, *et al.* Elucidating the role of preferential oxidation during ablation: Insights on the design and optimization of multicomponent ultra-high temperature ceramics. *J Adv Ceram* 2022, **11**: 1956–1975.
[61] Xiao JY, He PF, Xue L, *et al.* Hierarchical strain-modified medium-entropy carbide ceramics exhibit exceptional ablation resistance up to 2400 °C. *Adv Sci* 2026, **13**: 18785.
[62] Li JS, Zhang CR, Li B. Preparation and characterization of boron nitride coatings on carbon fibers from borazine by chemical vapor deposition. *Appl Surf Sci* 2011, **257**: 7752–7757.
[63] Li LH, Cervenka J, Watanabe K, *et al.* Strong oxidation resistance of atomically thin boron nitride nanosheets. *ACS Nano* 2014, **8**: 1457–1462.
[64] Hareesh R, Vetrivendan E, Balakrishnan S, *et al.* Oxidation mechanism and surface characterization of pyrolytic graphite in simulated air for pyrochemical reprocessing application. *J Nucl Mater* 2024, **593**: 154996.
[65] Knowles KM, Turan S. Boron nitride–silicon carbide interphase boundaries in silicon nitride–silicon carbide particulate composites. *J Eur Ceram Soc* 2002, **22**: 1587–1600.